

Compensating Spatiotemporally Inconsistent Observations for Online Dynamic 3D Gaussian Splatting

YOUNGSIK YUN, Yonsei University, Republic of Korea

JEONGMIN BAE, Yonsei University, Republic of Korea

HYUNSEUNG SON, Yonsei University, Republic of Korea

SEOHA KIM, Electronics and Telecommunications Research Institute, Republic of Korea

HAHYUN LEE, Electronics and Telecommunications Research Institute, Republic of Korea

GUN BANG, Electronics and Telecommunications Research Institute, Republic of Korea

YOUNGJUNG UH*, Yonsei University, Republic of Korea

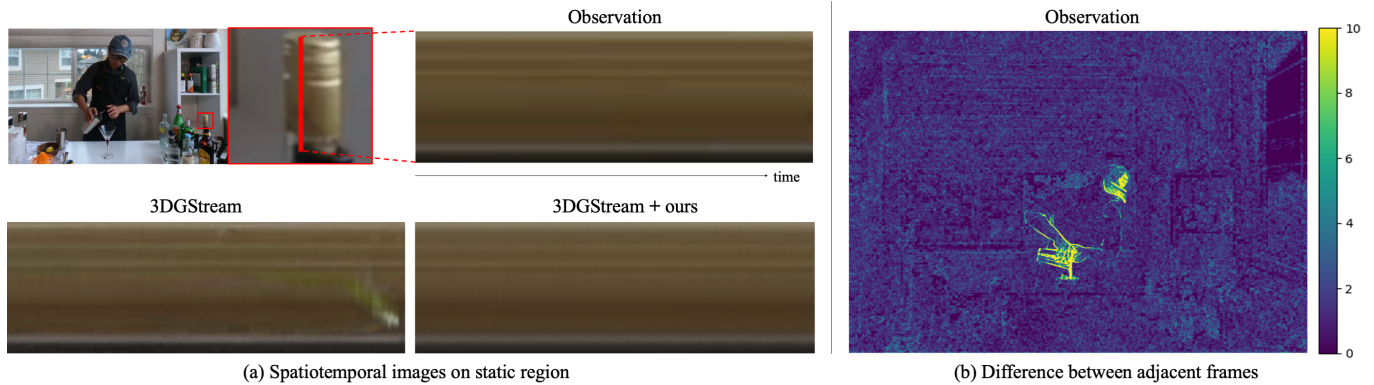


Fig. 1. **Overview.** (a) Previous online reconstruction methods are temporally inconsistent. To visualize it, we horizontally concatenate the fixed vertical line over time, creating spatiotemporal images. The previous method produces a noisy spatiotemporal image with artifacts in static regions, indicating temporal inconsistency. Our method enhances the temporal consistency of online reconstruction, producing a clearer spatiotemporal image. (b) The spatiotemporally inconsistent observations cause the temporal inconsistency. All real images contain errors such as noise and these errors vary across camera views and video frames. We visualize a heatmap measuring the difference between subsequent observation frames, indicating that the static regions are temporally inconsistent by the error. Most errors have values below 4 in 8-bit images, and these subtle, nearly imperceptible values affect online reconstruction methods, leading to temporal inconsistent results. To address this issue, we propose to restore the ideal scene by disregarding the errors.

Online reconstruction of dynamic scenes is significant as it enables learning scenes from live-streaming video inputs, while existing offline dynamic reconstruction methods rely on recorded video inputs. However, previous online reconstruction approaches have primarily focused on efficiency and rendering quality, overlooking the temporal consistency of their results,

*Corresponding author.

Authors' Contact Information: Youngsik Yun, Yonsei University, Seoul, Republic of Korea, bbangsik@yonsei.ac.kr; Jeongmin Bae, Yonsei University, Seoul, Republic of Korea, jaymin.bae@yonsei.ac.kr; Hyunseung Son, Yonsei University, Seoul, Republic of Korea, ghfod0917@yonsei.ac.kr; Seoha Kim, Electronics and Telecommunications Research Institute, Daejeon, Republic of Korea, hailey07@yonsei.ac.kr; Hahyun Lee, Electronics and Telecommunications Research Institute, Daejeon, Republic of Korea, hanilee@etri.re.kr; Gun Bang, Electronics and Telecommunications Research Institute, Daejeon, Republic of Korea, gbang@etri.re.kr; Youngjung Uh, Yonsei University, Seoul, Republic of Korea, yj.uh@yonsei.ac.kr.



This work is licensed under a Creative Commons Attribution 4.0 International License. *SIGGRAPH Conference Papers '25, Vancouver, BC, Canada*
 © 2025 Copyright held by the owner/author(s).
 ACM ISBN 979-8-4007-1540-2/2025/08
<https://doi.org/10.1145/3721238.3730678>

which often contain noticeable artifacts in static regions. This paper identifies that errors such as noise in real-world recordings affect temporal inconsistency in online reconstruction. We propose a method that enhances temporal consistency in online reconstruction from observations with temporal inconsistency which is inevitable in cameras. We show that our method restores the ideal observation by subtracting the learned error. We demonstrate that applying our method to various baselines significantly enhances both temporal consistency and rendering quality across datasets. Code, video results, and checkpoints are available at <https://bbangsik13.github.io/OR2>.

CCS Concepts: • **Computing methodologies** → **Reconstruction; Rendering; Rasterization; Point-based models.**

Additional Key Words and Phrases: online reconstruction, dynamic scene reconstruction, temporal consistency, streamable

ACM Reference Format:

Youngsik Yun, Jeongmin Bae, Hyunseung Son, Seoha Kim, Hahyun Lee, Gun Bang, and Youngjung Uh. 2025. Compensating Spatiotemporally Inconsistent Observations for Online Dynamic 3D Gaussian Splatting. In *Special Interest Group on Computer Graphics and Interactive Techniques Conference Conference Papers (SIGGRAPH Conference Papers '25)*, August 10–14, 2025, Vancouver, BC, Canada. ACM, New York, NY, USA, 13 pages. <https://doi.org/10.1145/3721238.3730678>

1 Introduction

Reconstructing dynamic scenes from multi-view videos is a crucial problem in computer vision and graphics to enable freely exploring novel viewpoints and timestamps. This capability has substantial potential for advancing applications in VR, AR, and XR. Neural Radiance Fields (NeRFs) [Mildenhall et al. 2020] have significantly improved the fidelity of 3D reconstruction, and have been adopted to dynamic scenes [Li et al. 2022b]. However, the relatively slow rendering speed of NeRFs hinders their use in real-time applications. Recent 3D Gaussian splatting (3DGS) [Kerbl et al. 2023] has advantages in rapid training and real-time rendering, making it a mainstream approach for dynamic scene reconstruction [Duan et al. 2024; Wu et al. 2024a; Yang et al. 2024b].

However, most dynamic scene reconstruction methods are limited to offline reconstruction, which relies on full access to video sequences. In addition, their results are typically not streamable, which cannot transmit part of the model of the specific moment to the user. Accordingly, they are incompatible with live-streaming applications, where only one frame is observable at a moment and the sent frames cannot be updated. Furthermore, the offline methods face out-of-memory issues with long videos and depend on hyperparameters specific to different lengths.

To reconstruct dynamic scenes from streaming video inputs and enable the streaming of a learned model, recent approaches reconstruct dynamic scenes in online configuration by consecutively optimizing a model which reconstructs a moment [Li et al. 2022a; Sun et al. 2024]. When the length of the video sequences is undefined, the online methods offer advantages over offline methods due to its unbounded nature [Wang et al. 2023a]. Furthermore, online methods do not rely on length-related hyperparameters. However, online reconstruction lacks temporal consistency in static regions, as shown in Figure 1a. We aim to produce temporally consistent and high quality results by finding the problem and solution.

First, we find that the observations bear unnoticeable error rather than capturing the ideal signal as shown in Figure 1b. Although we do not know the ideal signal, the colors in different moments at static regions should be the same, while the differences between adjacent frames are non-zero even at static regions. These errors are inevitable due to sensor noises or other reasons. By nature, they vary over time. We suggest that the online reconstruction produces temporally inconsistent results at static regions because it observes a frame at a moment and overfits to the time-varying errors. We demonstrate that the errors in the observation harm the temporal consistency through experiments on the synthetic dataset where we can prepare the observations with and without errors (Section 3.2).

To this end, we propose *observation-restoring online reconstruction* to reconstruct the ideal scene from imperfect observations with errors. The key idea is to reconstruct observations combining the Gaussians rendered on the images and residual maps which separately model the errors. We defer the details to Section 3.3. Combined with baselines, our method improves both temporal consistency and the quality of rendered results. The experiments cover various baselines and datasets. Additionally, our method reduces the number of Gaussians in the reconstruction leading to faster training and

rendering, and lower memory footprint. Lastly, the performance measures have lower variance across multiple runs of our method compared to the baselines, indicating stability of our method.

2 Related Work

In this section, we briefly review the literature on dynamic scene reconstruction using radiance fields, categorizing approaches into offline (Section 2.1) and online reconstruction (Section 2.2). Then, we discuss existing works reconstructing the radiance field from inaccurate observations (Section 2.3).

2.1 Offline Reconstruction of Radiance Fields

To extend NeRFs [Mildenhall et al. 2020] to reconstruct dynamic scenes, several approaches deform rays [Park et al. 2021a,b; Pumarola et al. 2021] or expand 3D representations to 4D [Cao and Johnson 2023; Fridovich-Keil et al. 2023], focusing on improving rendering performance, memory efficiency, and training speed. NeRF-Player [Song et al. 2023] enables the streaming of a learned model by representing each time of the scene with local feature channels.

The emergence of real-time rendering in 3D Gaussian Splatting (3DGS) [Kerbl et al. 2023] encourages extensive research in primitives-based dynamic scene reconstruction. Similar to Dynamic NeRFs, several works reconstruct dynamic scenes by deforming the Gaussians [Bae et al. 2025; Li et al. 2024b; Wu et al. 2024a] or extending 3D Gaussians to 4D Gaussians [Cho et al. 2024; Yang et al. 2024b].

Moreover, due to memory constraints, HyperReel [Attal et al. 2023] and STG [Li et al. 2024a] independently reconstruct each video segment from a single video sequence. This shows visual inconsistencies between the reconstructed results. SWinGS [Shaw et al. 2025] segments videos into size-varying segments based on motion intensity, sharing one frame between adjacent segments and training models for each segment. These models are subsequently fine-tuned across total frames to enhance temporal consistency.

However, these offline reconstruction methods cannot process live-streaming input, relying on recorded video input. Moreover, previous temporal consistency enhancement methods require full-frame fine-tuning which is unsuitable for online reconstruction.

2.2 Online Reconstruction of Radiance Fields

Online reconstruction methods sequentially optimize the scene at a given time, enabling live-streaming input processing and learned model streaming. The simplest way for online reconstruction is to train a model from each frame of live-streaming input. However, as most video contents contain significant redundancy across frames, reconstructing each frame independently is inefficient. Therefore, StreamRF [Li et al. 2022a] and ReRF [Wang et al. 2023a] consecutively learn the differences from previous frame for efficiency.

Recent research on online reconstruction predominantly uses 3D Gaussian Splatting (3DGS) as a representation for real-time rendering. These methods optimize the difference between consecutive frame models [Luiten et al. 2024]. To enhance training efficiency, 3DGStream [Sun et al. 2024] employs iNGP [Müller et al. 2022], an implicit network for optimizing the residual instead of directly optimizing Gaussian parameters. HiCoM [Gao et al. 2024] introduces

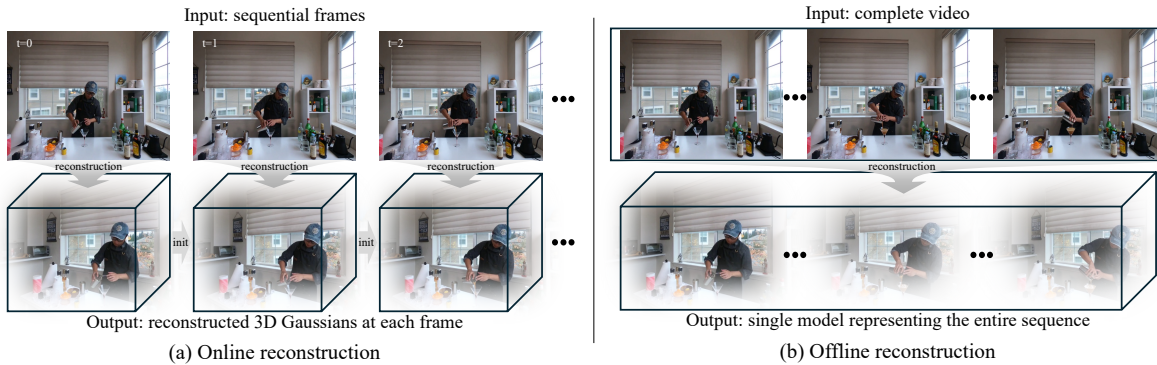


Fig. 2. **Comparison of Online and Offline Reconstruction.** (a) Online reconstruction takes streaming video as input and sequentially learns a model for each frame. (b) In contrast, offline reconstruction takes the complete set of video frames as input and produces a single model representing the entire sequence.

an explicit hierarchical motion field to reduce model capacity and utilizes a reference frame prediction to accelerate training.

However, these studies focus on the efficiency and visual quality of each frame, overlooking the temporal consistency of their results. We aim to enhance the temporal consistency of online reconstruction methods.

2.3 Optimizing Radiance Field from Imperfect Data

NeRF— [Wang et al. 2022], BARF [Lin et al. 2021], and SCNeRF [Jeong et al. 2021] jointly optimize NeRF and camera parameters, reducing the need for known camera parameters in static scene reconstruction. NoPe-NeRF [Bian et al. 2023], CF-3DGS [Fu et al. 2024] leverage depth priors for more accurate pose estimation. RoDyNeRF [Liu et al. 2023] extends this approach by jointly optimizing dynamic NeRF and camera parameters to correct inaccurate camera poses. SyncNeRF [Kim et al. 2024] jointly optimizes dynamic radiance fields and time offsets to reconstruct high-quality 4D models from unsynchronized videos.

DeblurNeRF [Ma et al. 2022], Deblur3DGS [Lee et al. 2025], Robust3DGaussians [Darmon et al. 2024], and BAD-Gaussians [Zhao et al. 2025] learn blur formation to obtain sharp reconstruction from blurry inputs. Deblur4DGS [Wu et al. 2024b] extends this concept to learning blur formation for sharp dynamic scene reconstruction from blurry monocular videos. DehazeNeRF [Chen et al. 2024], SeaSplat [Yang et al. 2024a], and DehazeGS [Yu et al. 2025] reconstruct a clean scene from hazy inputs. NeRF-W [Martin-Brualla et al. 2021], WildGaussians [Kulhanek et al. 2024], and NeRF-On-the-go [Ren et al. 2024] reconstruct 3D scenes from internet images by learning to ignore distractors, such as moving objects.

Sharing a key insight with our method, RawNeRF [Mildenhall et al. 2022] begins with the premise that all real images contain noise. RawNeRF demonstrates that NeRF can remove zero mean noise in the observation by averaging information using multi-view correspondence in high dynamic range (HDR) space. However, converting an HDR image where per-pixel noise follows zero-mean Gaussian distribution into a low dynamic range (LDR) image through nonlinear mapping alters the noise distribution, corrupting the noise distribution to a nonzero mean distribution. As a result, noise removal becomes less effective by averaging information in LDR images.

Several methods have attempted to reconstruct from inaccurate inputs, but they have generally focused on modeling errors under specific settings. In contrast, we address errors that occur naturally in real-world recording scenarios, where the error factors are diverse and ambiguous, making it challenging to model each factor separately.

3 Observation-Restoring Online Reconstruction

In this section, we first provide a preliminary of the online reconstruction of dynamic 3D Gaussian Splatting (Section 3.1). Next, we introduce our problem setting (Section 3.2). Finally, we propose its solution (Section 3). Algorithm 1 in the Appendix summarizes our method.

3.1 Preliminary: Online Dynamic 3D Gaussian Splatting

Offline reconstruction aims to optimize a single model representing the entire sequence from the entire duration of multi-view videos. In contrast, online reconstruction aims to reconstruct a model of a *moment* and update the model to sequentially reconstruct consecutive frames, for given sequentially captured multi-view images. This configuration is inevitable for live streaming free-viewpoint videos. Noting that the offline approaches assume a fixed duration for a model, the online configuration is advantageous for training long and arbitrary-length videos because the length of reconstruction increases while capturing a scene. Figure 2 conceptually compares online and offline reconstruction.

We provide a formal configuration. Let G_t be a set of Gaussians at time t , defined as $G_t = (\mu_t, \mathbf{q}_t, \mathbf{s}_t, \sigma_t, \mathbf{Y}_t)$ where μ , \mathbf{q} , \mathbf{s} , σ , and \mathbf{Y} denotes mean, rotation, scale, opacity, and spherical harmonics (SH) coefficients of the Gaussians, respectively¹. Given a set of cameras \mathbb{V} , let I_t^v be the observation of a scene from a camera $v \in \mathbb{V}$ at time $t \in \mathbb{Z}_{\geq 0}$ ².

The attributes of the Gaussians G_0 are initialized from Structure-from-Motion (SfM) points. These attributes are optimized by rendering G_0 across multiple cameras v , minimizing the loss between the rendered image I_0^v and their corresponding observation I_0^v . The

¹For brevity, we omit the indices of each Gaussian and its parameters.

² t is not bounded above in contrast to offline configuration.

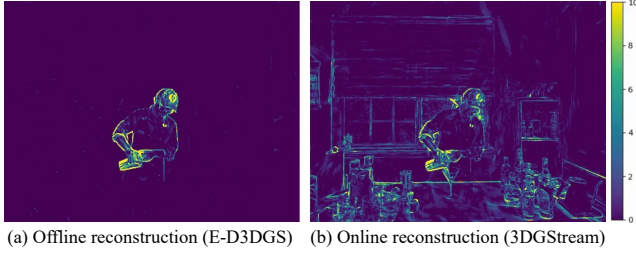


Fig. 3. **Differences between Consecutive Frames.** (a) While the offline reconstruction method maintains temporal consistency in static regions, (b) the online reconstruction method lacks temporal consistency.

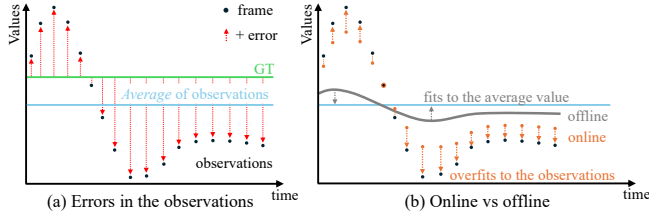


Fig. 4. **Conceptual Figure of the Problem Statement** (a) Each observation value contains errors added to the ground truth. (b) Due to limited data accessibility, online reconstruction tends to overfit each observation, whereas offline reconstruction converges to the global average over time.

number of Gaussians is adaptively adjusted by densification and pruning during optimization. Gaussians are split and cloned if their pixel-space gradient³ exceeds the predefined threshold, and pruned if their opacity is low. The Gaussians G_{t+1} at the next frame are obtained by deforming the attributes of the optimized G_t from the previous frame.

By design, deforming the Gaussians from previous frames cannot reconstruct new objects. Therefore, 3DGStream [Sun et al. 2024] introduces new Gaussians G_t^{new} to represent novel objects. However, 3DGStream uses these new Gaussians for a single frame and discard them, leading to temporally inconsistent results in dynamic regions (Appendix D.2). To solve this, similar to previous works [Gao et al. 2024; Girish et al. 2024], we propagate both new and deformed Gaussians to subsequent frames to enhance temporal consistency.

3.2 Problem Statement

Online reconstruction methods lack temporal consistency whereas offline reconstruction methods do not, as shown in Figure 3. Intriguingly, the observations lacks temporal consistency between adjacent frames even in static regions as shown in Figure 1b. We hypothesize that the observations are corrupted and do not ideally observe the original scene.

Offline reconstruction does not suffer from the above problem because the model converges to the average of all frames because the model with limited capacity cannot fit all tiny differences between the frames as shown in Figure 4. This averaging phenomenon ignores temporally varying errors in the observations, resulting in

³Gradient of the loss with respect to the coordinates projected on the image planes

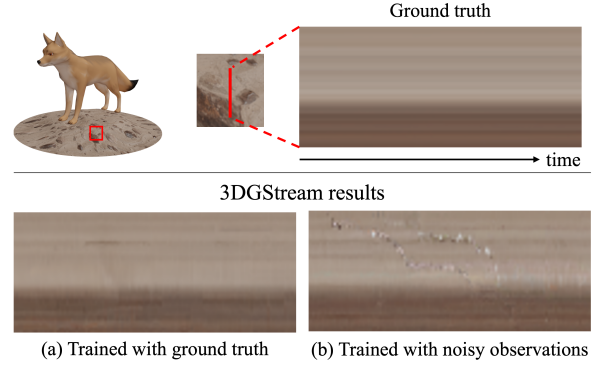


Fig. 5. **Comparison of Spatiotemporal Images under Two Settings.** (a) Training with ground truth images produces clearer results than (b) training with noisy observations created by adding noise to the ground truth. This demonstrates that noise harms the temporal consistency. ©DuDeHTM (CC BY-NC 4.0)

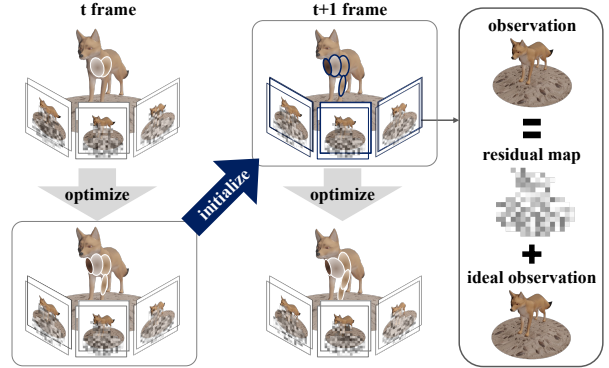


Fig. 6. **Framework.** We jointly optimize 3D Gaussians and residual maps for each camera view. The residual maps model observation errors. For subsequent frames, both Gaussians and residual maps are initialized with values from the previous frame. We model an observation as a combination of the ideal observation and residual map. ©DuDeHTM (CC BY-NC 4.0)

relatively consistent values for static regions. In contrast, online reconstruction converges to render a specific frame because it can access only the single target frame. As a result, the reconstructed result overfits the temporally varying errors in its corresponding observations, leading to temporally inconsistent reconstruction even in static regions.

We support the problem statement with a toy experiment. We reconstruct a synthetic dynamic 3D asset for given observations prepared by rendering it on fixed viewpoints, with and without noise⁴. While the results from ground truth observations are mostly clear (Figure 5a), the results from noisy observation exhibit flickering artifacts (Figure 5b).

We formulate the observations \tilde{I}_t^v capturing the scene as a combination of ideal observations I_t^v and errors M_t^v , and propose to

⁴We add Gaussian and Poisson noise.

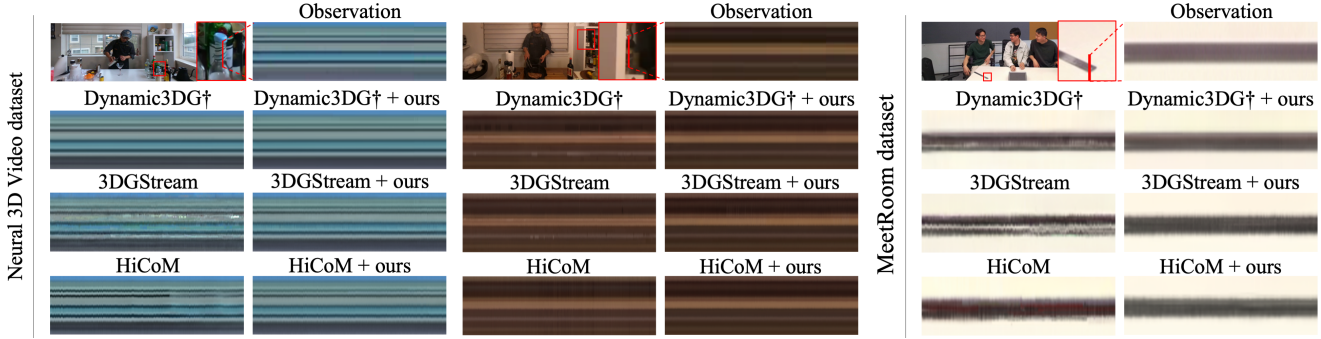


Fig. 7. **Qualitative Comparison on Neural 3D Video and MeetRoom Dataset.** Our method produces more temporal consistent spatiotemporal images.

restore the ideal scene with temporal consistency by disregarding the errors.

3.3 Decomposing Errors in the Observations

Learnable residual map. To address observations containing errors that vary across camera views v and frames t , we separately model these errors with additional residual maps $\hat{M}_t^v \in \mathbb{R}^{3 \times H \times W}$, which are optimized as learnable parameters during training:

$$\tilde{I}_t = I_t + M_t = \hat{I}_t + \hat{M}_t, \quad (1)$$

where \hat{I}_t and \hat{M}_t are rendered image and estimated residual, respectively, and we omit v for brevity. H and W denote the height and width of the image I_t . During optimization, we minimize the difference between \tilde{I}_t and $\hat{I}_t + \hat{M}_t$ by jointly updating G_t and \hat{M}_t . An optimization step becomes:

$$G_t, \hat{M}_t \leftarrow \text{Adam}(\nabla L_{\text{total}}(\tilde{I}_t, \hat{I}_t + \hat{M}_t)), \quad (2)$$

where L_{total} will be described later.

Separately modeling the residual maps restores the ideal observations as follows. In Eq. 1, we expect the rendered images and the estimated residual maps to match the corrupted observation together. Fitting multi-view inconsistent high-frequency noise with a residual maps are easier than optimizing one set of Gaussians. Moreover, learning multi-view and temporal inconsistent noise with a residual map is easier than fine-tuning a well-trained Gaussians from the previous frame. As a result, the optimized Gaussians reconstruct the true scene without corruption. I.e., the rendered images become the ideal observation without errors.

First Frame Reconstruction. To reconstruct the first frame, we initialize Gaussians from SfM points [Schonberger and Frahm 2016] and residual maps to zero. We then jointly optimize them same as 3DGS [Kerbl et al. 2023]. To prevent the residual maps from dominating the reconstruction, they are frozen at zero until the Gaussians start densification.

In addition, we apply L1 regularization on opacity [Bae et al. 2025; Kheradmand et al. 2024] as resetting opacity in 3DGS [Kerbl et al. 2023] disrupts stable optimization of the residual maps: $L_{\text{opa}} = \sum_i \|\sigma_t^i\|_1$, where σ_t^i denotes opacity of the i -th Gaussian at time t . We also employ L1 regularization on the residual map to prevent overfitting to view-conditioned color: $L_{\text{res}} = \|\hat{M}_t^v\|_1$.

The total loss for the first frame is:

$$L_{\text{total}} = (1 - \lambda)L_1 + \lambda L_{\text{D-SSIM}} + \lambda_{\text{opa}}L_{\text{opa}} + \lambda_{\text{res}}L_{\text{res}}. \quad (3)$$

Sequential Frame Reconstruction. We consecutively propagate new Gaussians across subsequent frames: $G_{t+1} \leftarrow (G_t, G_t^{\text{new}})$ because using the new Gaussians in only a single frame and discarding them harms the temporal consistency. We do not use L_{opa} in sequential frame reconstruction to ensure fair comparison with baselines. Finally, the total loss for the remaining frames is:

$$L_{\text{total}} = (1 - \lambda)L_1 + \lambda L_{\text{D-SSIM}} + \lambda_{\text{res}}L_{\text{res}}. \quad (4)$$

4 Experiment

In this section, we first provide the reasons for choosing the dataset, implementation, and the evaluation metrics (Section 4.1). Next, we demonstrate our improvements in both temporal consistency and visual quality upon the baselines (Section 4.2). We then show our proposed method effectively restores the observations (Section 4.3). Finally, we conduct an ablation study to assess the performance of our method (Section 4.4).

4.1 Datasets, Implementation, and Metrics

4.1.1 Datasets. Following the prior works [Luiten et al. 2024; Sun et al. 2024], we use undistorted images and SfM points in our experiments. Additional experiments on the original images and MVS points [Gao et al. 2024; Wu et al. 2024a] are detailed in Appendix C. We evaluated the baselines on these datasets.

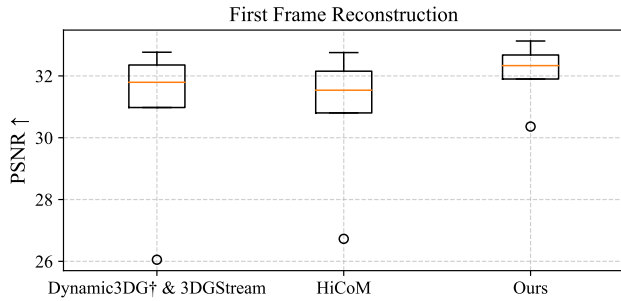
Neural 3D Video [Li et al. 2022b]. The dataset contains six scenes captured by 17 to 21 multi-view cameras over 300 frames. Following the prior works [Fridovich-Keil et al. 2023; Wang et al. 2023b], we downsample the video by a factor of two and remove the unsynchronized video in coffee_martini scene.

MeetRoom [Li et al. 2022a]. The dataset contains three scenes captured by 14 multi-view cameras over 300 frames.

Sync-NeRF [Kim et al. 2024]. The dataset is rendered from dynamic 3D asset with static regions, providing a training dataset without errors (ground truth dataset). For our experiments, we use

Table 1. **Average Performance on Neural 3D Video and MeetRoom Dataset.** Computational cost was measured on flame_salmon with RTX A5000.

Model	Neural 3D Video			MeetRoom			Computational Cost	
	PSNR \uparrow	SSIM \uparrow	mTV $\times 100$ \downarrow	PSNR \uparrow	SSIM \uparrow	mTV $\times 100$ \downarrow	# Gaussians \downarrow	Training time \downarrow
Dynamic3DG \dagger	32.48	0.960	0.153	30.79	0.952	0.175	315K	136. sec/frame
Dynamic3DG \dagger + ours	33.03	0.961	0.053	31.29	0.953	0.126	246K	130. sec/frame
3DGStream	32.58	0.960	0.178	31.78	0.955	0.049	315K	13.3 sec/frame
3DGStream + ours	33.13	0.961	0.103	32.29	0.957	0.024	268K	13.1 sec/frame
HiCoM	32.09	0.956	0.164	29.42	0.936	0.127	307K	11.0 sec/frame
HiCoM + ours	32.46	0.957	0.118	29.48	0.938	0.045	218K	10.2 sec/frame

Fig. 8. **First Frame Reconstruction.** Box plots comparing first frame reconstruction quality across 10 runs for each scene in the Neural 3D Video dataset.

the modified fox⁵ scene (see Appendix B.3 for details). We train with noisy observations¹ and evaluate against the ground truth.

4.1.2 Implementation. We apply our method to the state-of-the-art online reconstruction methods (Dynamic3DG [Luiten et al. 2024], 3DGStream [Sun et al. 2024], and HiCoM [Gao et al. 2024]) and compare the performance with the original implementations. StreamRF [Li et al. 2022a] is excluded because it is hardly reproducible.

We follow the official implementations except for Dynamic3DG. Due to the poor results of Dynamic3DG on the datasets with forward-facing configuration, we modified it to improve performance, naming it Dynamic3DG \dagger (see Appendix B.1 for details). To ensure a fair comparison, we apply our method to HiCoM using the same pruning strategy proposed in it⁶.

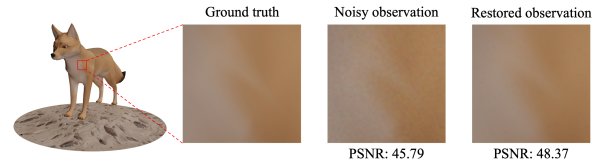
As 3DGS [Kerbl et al. 2023] has randomness in optimization⁷, we select the 3D Gaussians with the highest PSNR from 10 runs as the initialization for reconstructing the sequential frame. This protocol is confirmed by correspondence with the authors of 3DGStream. We use the same 3D Gaussians at the first frame for both Dynamic3DG \dagger and 3DGStream⁸.

⁵©DuDeHTM (CC BY-NC 4.0)

⁶HiCoM maintains compactness by pruning the K lowest opacity Gaussians from the combined set of deformed and new Gaussians, where K equals the number of new Gaussians. However, this pruning strategy degrades visual quality.

⁷Please refer to <https://github.com/graphdeco-inria/gaussian-splatting/issues/89>

⁸Note that once the 3D Gaussians at the first frame are fixed, sequential frames bear minimal variance, indicating that the randomness in online reconstruction primarily derives from the first frame.

Fig. 9. **Observation Restoration.** Our learned residual maps successfully restore the noisy observations. ©DuDeHTM (CC BY-NC 4.0)

In our experiments, we do not prune Gaussians with large radii in pixel-space because it degrades performance. We set the SH degree to 3 when applying our method (See Section 4.4).

4.1.3 Metrics. We report the quality of rendered images using Peak Signal-to-Noise Ratio (PSNR), Structural Similarity Index Measure (SSIM), and masked Total Variation (mTV). PSNR quantifies pixel color error between the rendered video and the test dataset. We measure SSIM to account for the perceived similarity of the rendered image. Additionally, we measure mTV to measure temporal consistency in static regions indicated by predefined masks. Appendix B.3 provides details about the masks used in the experiments. Higher PSNR and SSIM values and lower mTV values indicate better visual quality. For readability, we multiply mTV by 100 and refer to it as mTV $\times 100$.

4.2 Comparison on Real-world Dataset

4.2.1 Visual Quality.

The First Frame. Our method improves PSNR at the first frame in both median and highest values as shown in Figure 8. The box plot is drawn with 10 runs per scene in the Neural 3D Video dataset. In addition, our method achieve lower variance, implying higher stability than the baselines.

All Frames. Consecutively applying our method to all frames improves both PSNR and SSIM, achieving superior visual quality as shown in Table 1.

4.2.2 Temporal Consistency. Figure 7 presents spatiotemporal images of static areas. While baseline methods show noisy results, combining our method produces clear outputs, indicating improved temporal consistency. In Table 1, applying our method reduces mTV, demonstrating enhanced temporal consistency.

Table 2. Average Performance on Sync-NeRF Dataset.

Model	PSNR \uparrow	SSIM \uparrow	mTV $\times 100$ \downarrow
3DGStream	38.79	0.982	0.483
3DGStream on denoised observations	38.63	0.979	0.417
3DGStream + ours	39.16	0.987	0.318

Table 3. Quantitative Comparison of Ablation Study.

Method	PSNR \uparrow	SSIM \uparrow	mTV $\times 100$ \downarrow
3DGStream + ours	33.13	0.961	0.103
w/o residual maps	32.65	0.960	0.161
w/o SH degree 3	33.08	0.961	0.129
w/o reuse new Gaussians	33.06	0.960	0.118

4.2.3 *Computational Cost.* Table 1 shows the computational costs. Our approach reduces the number of Gaussians for each baselines. Although we optimize additional parameters, the reduced number of Gaussians decreases the training time. Notably, the residual maps are only used during training and are not stored.

4.3 Comparison on Synthetic Dataset

4.3.1 *Restoration.* To demonstrate the ability of our learned residual map to restore the observations, we conduct experiments on Sync-NeRF dataset. We restore the train view observation to its ground truth by subtracting the residual map from the corresponding observation. This restoration increases PSNR (+2.58) with clear visual quality, as shown in Figure 9.

4.3.2 *Comparison to Preprocessing.* We additionally compare our method against combination of 3DGStream and a denoising model [Liang et al. 2024], where 3DGStream reconstructs the scene from the denoised observations.

As shown in Table 2, our method outperforms competitors in both visual quality (PSNR) and temporal consistency (mTV). Using a denoising model also enhances temporal consistency, which supports our problem settings. Nonetheless, its effectiveness remains lower than ours⁹.

4.4 Ablation Study

4.4.1 *Learnable Residual Maps.* To validate the effect of the residual map, we compared “3DGStream + ours” to a version without the residual map, labeling “w/o residual maps”. As shown in Table 2, using residual maps improves both temporal consistency (reduced mTV) and visual quality (increased PSNR). Our method reduces unnecessary Gaussians by separating observation errors that inflate the pixel-space gradient. Leveraging our residual maps decreases the number of Gaussians, reducing G_0 to $0.69\times$ and G_t^{new} to $0.28\times$, as shown in Figure 10.

4.4.2 *SH Degree.* We analyze the variation of reconstruction performance due to different SH degrees. The higher the SH degrees,

⁹Moreover, Liang et al. [2024] degrade visual quality through over-smoothing, and the preprocessing time (196 seconds per frame) significantly exceeds the sequential frame reconstruction time (6 seconds per frame).

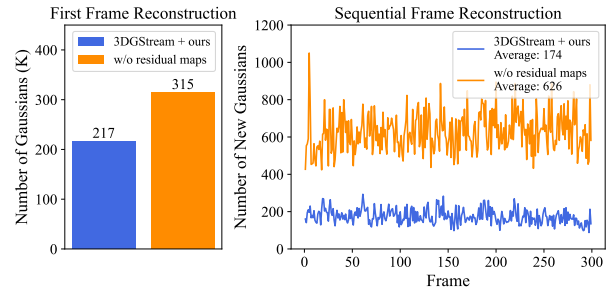


Fig. 10. Ablation Study of Residual Maps. Our proposed residual maps reduces the number of Gaussians in both first frame reconstruction and subsequent new Gaussian additions, measured on the flame_salmon scene.

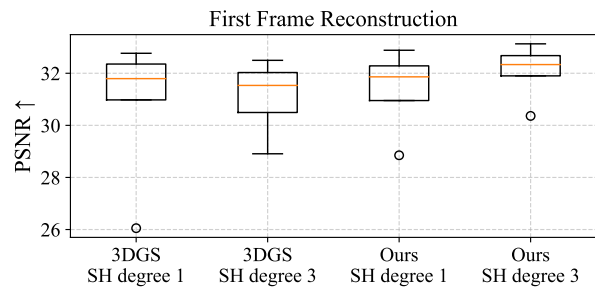


Fig. 11. Ablation Study of SH Degree. Difference in first frame reconstruction quality between 3DGS and ours based on SH degree.

the higher the model capacity. In the first frame reconstruction, 3DGS [Kerbl et al. 2023] with higher model capacity tends to overfit observation errors, performing better at SH degree 1, as shown in Figure 11. In contrast, our residual maps fit these errors instead of SH, allowing Gaussians to effectively use their higher model capacity without overfitting the errors. Moreover, higher 3D Gaussian capacity prevents residual maps from overfitting view-dependent color, thus achieving superior performance at SH degree 3. Consequently, in sequential frame reconstruction, setting the SH degree to 3 enhances visual quality and temporal consistency compared to lower SH degree 1, as demonstrated in Table 3 “w/o SH degree 3”.

4.4.3 *New Gaussians.* Propagating new and deformed Gaussians to the next frame enhances visual quality and temporal consistency in static regions compared to using new Gaussians only in specific frames labeled as “w/o reuse new Gaussians” in Table 3. In the Appendix D.2, we further discuss the enhancement of temporal consistency in dynamic regions.

5 Conclusion

In this paper, we reveal that the previous online reconstruction methods do not produce temporally consistent results. One of the causes of this problem is the errors in the observations. We resolve the problem by decomposing the rendered images into the ideal signal and the errors during the optimization. Our method significantly improves temporal consistency and visual quality.



Fig. 12. **Limitation.** Although our method improves the baselines, it does not fix the artifacts due to fast motion.

Limitation. Existing baselines struggle under challenging conditions such as motion blur, sparse viewpoints, severe noise, and fast motion. As these failures arise from problem settings that are orthogonal to our temporal consistency objective, our method does not resolve these failures (Figure 12). Moreover, since our method assumes well-reconstructed scenes, its effectiveness decreases in these scenarios (Appendix D.4-D.5). However, our method will remain effective in improving temporal consistency when integrated with future work that improves upon these baselines.

In addition, a more in-depth analysis of potential causes of temporal inconsistency beyond noise, as well as the impact of various types of noise is needed, which we leave for future work.

Acknowledgments

This work is supported by the Institute for Information & Communications Technology Planning & Evaluation (IITP) grant funded by the Korea government(MSIT) (No. 2017-0-00072, Development of Audio/Video Coding and Light Field Media Fundamental Technologies for Ultra Realistic Tera-media)

References

- Benjamin Attal, Jia-Bin Huang, Christian Richardt, Michael Zollhöfer, Johannes Kopf, Matthew O’Toole, and Changil Kim. 2023. HyperReel: High-Fidelity 6-DoF Video With Ray-Conditioned Sampling. In *Proceedings of the IEEE/CVF Conference on Computer Vision and Pattern Recognition (CVPR)*. IEEE, Vancouver, BC, Canada, 16610–16620.
- Jeongmin Bae, Seoha Kim, Youngsik Yun, Hahyun Lee, Gun Bang, and Youngjung Uh. 2025. Per-Gaussian Embedding-Based Deformation for Deformable 3D Gaussian Splatting. In *Computer Vision – ECCV 2024*, Aleš Leonardis, Elisa Ricci, Stefan Roth, Olga Russakovsky, Torsten Sattler, and Gül Varol (Eds.), Springer Nature Switzerland, Cham, 321–335.
- Wenjing Bian, Zirui Wang, Kejie Li, Jia-Wang Bian, and Victor Adrian Prisacariu. 2023. NoPe-NeRF: Optimising Neural Radiance Field With No Pose Prior. In *Proceedings of the IEEE/CVF Conference on Computer Vision and Pattern Recognition (CVPR)*. IEEE, Vancouver, BC, Canada, 4160–4169.
- Ang Cao and Justin Johnson. 2023. HexPlane: A Fast Representation for Dynamic Scenes. In *Proceedings of the IEEE/CVF Conference on Computer Vision and Pattern Recognition (CVPR)*. IEEE, Vancouver, BC, Canada, 130–141.
- Wei-Ting Chen, Wang Yifan, Sy-Yen Kuo, and Gordon Wetzstein. 2024. DehazeNeRF: Multi-image Haze Removal and 3D Shape Reconstruction using Neural Radiance Fields. In *2024 International Conference on 3D Vision (3DV)*. IEEE, Davos, Switzerland, 247–256. <https://doi.org/10.1109/3DV62453.2024.00039>
- Woong Oh Cho, In Cho, Seoha Kim, Jeongmin Bae, Youngjung Uh, and Seon Joo Kim. 2024. 4D Scaffold Gaussian Splatting for Memory Efficient Dynamic Scene Reconstruction. arXiv:2411.17044 [cs.CV] <https://arxiv.org/abs/2411.17044>
- François Darmon, Lorenzo Porzi, Samuel Rota-Bulò, and Peter Kotschieder. 2024. Robust Gaussian Splatting. arXiv:2404.04211 [cs.CV] <https://arxiv.org/abs/2404.04211>
- Yuanxing Duan, Fangyin Wei, Qiyu Dai, Yuhang He, Wenzheng Chen, and Baoquan Chen. 2024. 4D-Rotor Gaussian Splatting: Towards Efficient Novel View Synthesis for Dynamic Scenes. In *ACM SIGGRAPH 2024 Conference Papers* (Denver, CO, USA) (SIGGRAPH ’24). Association for Computing Machinery, New York, NY, USA, Article 87, 11 pages. <https://doi.org/10.1145/3641519.3657463>
- Sara Fridovich-Keil, Giacomo Meanti, Frederik Rahbæk Warburg, Benjamin Recht, and Angjoo Kanazawa. 2023. K-Planes: Explicit Radiance Fields in Space, Time, and Appearance. In *Proceedings of the IEEE/CVF Conference on Computer Vision and Pattern Recognition (CVPR)*. IEEE, Vancouver, BC, Canada, 12479–12488.
- Yang Fu, Sifei Liu, Amey Kulkarni, Jan Kautz, Alexei A. Efros, and XiaoLong Wang. 2024. COLMAP-Free 3D Gaussian Splatting. In *Proceedings of the IEEE/CVF Conference on Computer Vision and Pattern Recognition (CVPR)*. IEEE, Seattle, Washington, USA, 20796–20805.
- Qiankun Gao, Jiarui Meng, Chengxiang Wen, Jie Chen, and Jian Zhang. 2024. HiCoM: Hierarchical Coherent Motion for Dynamic Streamable Scenes with 3D Gaussian Splatting. In *Advances in Neural Information Processing Systems*, A. Globerson, L. Mackey, D. Belgrave, A. Fan, U. Paquet, J. Tomczak, and C. Zhang (Eds.), Vol. 37. Curran Associates, Inc., Vancouver, BC, Canada, 80609–80633. https://proceedings.neurips.cc/paper_files/paper/2024/file/9370cc8d438b9ed8cb4344818a251d9a-Paper-Conference.pdf
- Sharath Girish, Tianye Li, Amrita Mazumdar, Abhinav Shrivastava, David Luebke, and Shalini De Mello. 2024. QUEEN: QUantized Efficient ENcoding of Dynamic Gaussians for Streaming Free-viewpoint Videos. In *Advances in Neural Information Processing Systems*, A. Globerson, L. Mackey, D. Belgrave, A. Fan, U. Paquet, J. Tomczak, and C. Zhang (Eds.), Vol. 37. Curran Associates, Inc., Vancouver, BC, Canada, 43435–43467. https://proceedings.neurips.cc/paper_files/paper/2024/file/4c9477b9e2c7ec0ad3f4f15077aaf85a-Paper-Conference.pdf
- Yoonwoo Jeong, Seokjun Ahn, Christopher Choy, Anima Anandkumar, Minsu Cho, and Jaesik Park. 2021. Self-Calibrating Neural Radiance Fields. In *Proceedings of the IEEE/CVF International Conference on Computer Vision (ICCV)*. IEEE, Virtual, 5846–5854.
- Bernhard Kerbl, Georgios Kopanas, Thomas Leimkuehler, and George Drettakis. 2023. 3D Gaussian Splatting for Real-Time Radiance Field Rendering. *ACM Trans. Graph.* 42, 4, Article 139 (July 2023), 14 pages. <https://doi.org/10.1145/3592433>
- Shakiba Kheradmand, Daniel Reibain, Gopal Sharma, Weiwei Sun, Yang-Che Tseng, Hossam Isack, Abhishek Kar, Andrea Tagliasacchi, and Kwang Moo Yi. 2024. 3D Gaussian Splatting as Markov Chain Monte Carlo. In *Advances in Neural Information Processing Systems*, A. Globerson, L. Mackey, D. Belgrave, A. Fan, U. Paquet, J. Tomczak, and C. Zhang (Eds.), Vol. 37. Curran Associates, Inc., Vancouver, Canada, 80965–80986. https://proceedings.neurips.cc/paper_files/paper/2024/file/93be245fce00a9bb2333c17ceae4b732-Paper-Conference.pdf
- Seoha Kim, Jeongmin Bae, Youngsik Yun, Hahyun Lee, Gun Bang, and Youngjung Uh. 2024. Sync-NeRF: Generalizing Dynamic NeRFs to Unsynchronized Videos. *Proceedings of the AAAI Conference on Artificial Intelligence* 38 (03 2024), 2777–2785. <https://doi.org/10.1609/aaai.v38i3.28057>
- Jonas Kulhanek, Songyou Peng, Zuzana Kukekova, Marc Pollefeys, and Torsten Sattler. 2024. WildGaussians: 3D Gaussian Splatting In the Wild. In *Advances in Neural Information Processing Systems*, A. Globerson, L. Mackey, D. Belgrave, A. Fan, U. Paquet, J. Tomczak, and C. Zhang (Eds.), Vol. 37. Curran Associates, Inc., Vancouver, BC, Canada, 21271–21288. https://proceedings.neurips.cc/paper_files/paper/2024/file/25c0fe7b157821dd3140727dc07461da-Paper-Conference.pdf
- Byeonghyeon Lee, Howoong Lee, Xiangyu Sun, Usman Ali, and Eunbyung Park. 2025. Deblurring 3D Gaussian Splatting. In *Computer Vision – ECCV 2024*, Aleš Leonardis, Elisa Ricci, Stefan Roth, Olga Russakovsky, Torsten Sattler, and Gül Varol (Eds.), Springer Nature Switzerland, Cham, 127–143.
- Deqi Li, Shi-Sheng Huang, Zhiyuan Lu, Xinran Duan, and Hua Huang. 2024b. ST-4DGS: Spatial-Temporally Consistent 4D Gaussian Splatting for Efficient Dynamic Scene Rendering. In *ACM SIGGRAPH 2024 Conference Papers* (Denver, CO, USA) (SIGGRAPH ’24). Association for Computing Machinery, New York, NY, USA, Article 83, 11 pages. <https://doi.org/10.1145/3641519.3657520>
- Lingzhi Li, Zhen Shen, Zhongshu Wang, Li Shen, and Ping Tan. 2022a. Streaming Radiance Fields for 3D Video Synthesis. In *Advances in Neural Information Processing Systems*, S. Koyejo, S. Mohamed, A. Agarwal, D. Belgrave, K. Cho, and A. Oh (Eds.), Vol. 35. Curran Associates, Inc., New Orleans, Louisiana, USA, 13485–13498. https://proceedings.neurips.cc/paper_files/paper/2022/file/57c2c952f388f6185db98f441351c96-Paper-Conference.pdf
- Tianye Li, Mira Slavcheva, Michael Zollhöfer, Simon Green, Christoph Lassner, Changil Kim, Tanner Schmidt, Steven Lovegrove, Michael Goesele, Richard Newcombe, and ZhaoYang Lv. 2022b. Neural 3D Video Synthesis From Multi-View Video. In *Proceedings of the IEEE/CVF Conference on Computer Vision and Pattern Recognition (CVPR)*. IEEE, New Orleans, Louisiana, USA, 5521–5531.
- Zhan Li, Zhang Chen, Zhong Li, and Yi Xu. 2024a. Spacetime Gaussian Feature Splatting for Real-Time Dynamic View Synthesis. In *Proceedings of the IEEE/CVF Conference on Computer Vision and Pattern Recognition (CVPR)*. IEEE, Seattle, Washington, USA, 8508–8520.
- Jingyun Liang, Jiezhang Cao, Yuchen Fan, Kai Zhang, Rakesh Ranjan, Yawei Li, Radu Timofte, and Luc Van Gool. 2024. VRT: A Video Restoration Transformer. *Trans. Img. Proc.* 33 (Jan. 2024), 2171–2182. <https://doi.org/10.1109/TIP.2024.3372454>
- Chen-Hsuan Lin, Wei-Chiu Ma, Antonio Torralba, and Simon Lucey. 2021. BARF: Bundle-Adjusting Neural Radiance Fields. In *Proceedings of the IEEE/CVF International Conference on Computer Vision (ICCV)*. IEEE, Virtual, 5741–5751.
- Yu-Lun Liu, Chen Gao, Andréas Meuleman, Hung-Yu Tseng, Ayush Saraf, Changil Kim, Yung-Yu Chuang, Johannes Kopf, and Jia-Bin Huang. 2023. Robust Dynamic

- Radiance Fields. In *Proceedings of the IEEE/CVF Conference on Computer Vision and Pattern Recognition (CVPR)*. IEEE, Vancouver, BC, Canada, 13–23.
- Jonathon Luiten, Georgios Kopanas, Bastian Leibe, and Deva Ramanan. 2024. Dynamic 3D Gaussians: Tracking by Persistent Dynamic View Synthesis. In *2024 International Conference on 3D Vision (3DV)*. IEEE, Davos, Switzerland, 800–809. <https://doi.org/10.1109/3DV62453.2024.00044>
- Li Ma, Xiaoyu Li, Jing Liao, Qi Zhang, Xuan Wang, Jue Wang, and Pedro V. Sander. 2022. Deblur-NeRF: Neural Radiance Fields From Blurry Images. In *Proceedings of the IEEE/CVF Conference on Computer Vision and Pattern Recognition (CVPR)*. IEEE, New Orleans, Louisiana, USA, 12861–12870.
- Ricardo Martin-Brualla, Noha Radwan, Mehdi S. M. Sajjadi, Jonathan T. Barron, Alexey Dosovitskiy, and Daniel Duckworth. 2021. NeRF in the Wild: Neural Radiance Fields for Unconstrained Photo Collections. In *Proceedings of the IEEE/CVF Conference on Computer Vision and Pattern Recognition (CVPR)*. IEEE, Virtual, 7210–7219.
- Ben Mildenhall, Peter Hedman, Ricardo Martin-Brualla, Pratul P. Srinivasan, and Jonathan T. Barron. 2022. NeRF in the Dark: High Dynamic Range View Synthesis From Noisy Raw Images. In *Proceedings of the IEEE/CVF Conference on Computer Vision and Pattern Recognition (CVPR)*. IEEE, New Orleans, Louisiana, USA, 16190–16199.
- Ben Mildenhall, Pratul P. Srinivasan, Matthew Tancik, Jonathan T. Barron, Ravi Ramamoorthi, and Ren Ng. 2020. NeRF: Representing Scenes as Neural Radiance Fields for View Synthesis. In *Computer Vision – ECCV 2020*, Andrea Vedaldi, Horst Bischof, Thomas Brox, and Jan-Michael Frahm (Eds.). Springer International Publishing, Cham, 405–421.
- Thomas Müller, Alex Evans, Christoph Schied, and Alexander Keller. 2022. Instant Neural Graphics Primitives with a Multiresolution Hash Encoding. *ACM Trans. Graph.* 41, 4, Article 102 (July 2022), 15 pages. <https://doi.org/10.1145/3528223.3530127>
- Keunhong Park, Utkarsh Sinha, Jonathan T. Barron, Sofien Bouaziz, Dan B Goldman, Steven M. Seitz, and Ricardo Martin-Brualla. 2021a. Nerfies: Deformable Neural Radiance Fields. In *Proceedings of the IEEE/CVF International Conference on Computer Vision (ICCV)*. IEEE, Virtual, 5865–5874.
- Keunhong Park, Utkarsh Sinha, Peter Hedman, Jonathan T. Barron, Sofien Bouaziz, Dan B Goldman, Ricardo Martin-Brualla, and Steven M. Seitz. 2021b. HyperNeRF: a higher-dimensional representation for topologically varying neural radiance fields. *ACM Trans. Graph.* 40, 6, Article 238 (Dec. 2021), 12 pages. <https://doi.org/10.1145/3478513.3480487>
- Albert Pumarola, Enric Corona, Gerard Pons-Moll, and Francesc Moreno-Noguer. 2021. D-NeRF: Neural Radiance Fields for Dynamic Scenes. In *Proceedings of the IEEE/CVF Conference on Computer Vision and Pattern Recognition (CVPR)*. IEEE, Virtual, 10318–10327.
- Weining Ren, Zihan Zhu, Boyang Sun, Jiaqi Chen, Marc Pollefeys, and Songyou Peng. 2024. NeRF On-the-go: Exploiting Uncertainty for Distractor-free NeRFs in the Wild. In *Proceedings of the IEEE/CVF Conference on Computer Vision and Pattern Recognition (CVPR)*. IEEE, Seattle, Washington, USA, 8931–8940.
- Johannes L Schonberger and Jan-Michael Frahm. 2016. Structure-from-motion revisited. In *Proceedings of the IEEE conference on computer vision and pattern recognition*. IEEE, Las Vegas, USA, 4104–4113.
- Richard Shaw, Michal Nazarczuk, Jifei Song, Arthur Moreau, Sibi Catley-Chandar, Helisa Dharmo, and Eduardo Pérez-Pellitero. 2025. SWinGS: Sliding Windows for Dynamic 3D Gaussian Splatting. In *Computer Vision – ECCV 2024*, Aleš Leonardis, Elisa Ricci, Stefan Roth, Olga Russakovsky, Torsten Sattler, and Gül Varol (Eds.). Springer Nature Switzerland, Cham, 37–54.
- Liangchen Song, Anpei Chen, Zhong Li, Zhang Chen, Lele Chen, Junsong Yuan, Yi Xu, and Andreas Geiger. 2023. Nerfplayer: A streamable dynamic scene representation with decomposed neural radiance fields. *IEEE Transactions on Visualization and Computer Graphics* 29, 5 (2023), 2732–2742.
- Jiakai Sun, Han Jiao, Guangyuan Li, Zhanjie Zhang, Lei Zhao, and Wei Xing. 2024. 3DGStream: On-the-Fly Training of 3D Gaussians for Efficient Streaming of Photo-Realistic Free-Viewpoint Videos. In *Proceedings of the IEEE/CVF Conference on Computer Vision and Pattern Recognition (CVPR)*. IEEE, Seattle, Washington, USA, 20675–20685.
- Feng Wang, Sinan Tan, Xinghang Li, Zeyue Tian, Yafei Song, and Huaping Liu. 2023b. Mixed Neural Voxels for Fast Multi-view Video Synthesis. In *Proceedings of the IEEE/CVF International Conference on Computer Vision (ICCV)*. IEEE, Paris, France, 19706–19716.
- Liao Wang, Qiang Hu, Qihan He, Ziyu Wang, Jingyi Yu, Tinne Tuytelaars, Lan Xu, and Minye Wu. 2023a. Neural Residual Radiance Fields for Streamably Free-Viewpoint Videos. In *Proceedings of the IEEE/CVF Conference on Computer Vision and Pattern Recognition (CVPR)*. IEEE, Vancouver, BC, Canada, 76–87.
- Penghao Wang, Zhirui Zhang, Liao Wang, Kaixin Yao, Siyuan Xie, Jingyi Yu, Minye Wu, and Lan Xu. 2024. V3: Viewing Volumetric Videos on Mobiles via Streamable 2D Dynamic Gaussians. *ACM Trans. Graph.* 43, 6, Article 187 (Nov. 2024), 13 pages. <https://doi.org/10.1145/3687935>
- Zirui Wang, Shangzhe Wu, Weidi Xie, Min Chen, and Victor Adrian Prisacariu. 2022. NeRF-: Neural Radiance Fields Without Known Camera Parameters. arXiv:2102.07064 [cs.CV] <https://arxiv.org/abs/2102.07064>
- Guanjun Wu, Taoran Yi, Jiemin Fang, Lingxi Xie, Xiaoqiang Zhang, Wei Wei, Wenyu Liu, Qi Tian, and Xinggang Wang. 2024a. 4D Gaussian Splatting for Real-Time Dynamic Scene Rendering. In *Proceedings of the IEEE/CVF Conference on Computer Vision and Pattern Recognition (CVPR)*. IEEE, Seattle, Washington, USA, 20310–20320.
- Renlong Wu, Zhilu Zhang, Mingyang Chen, Xiaoqiang Fan, Zifei Yan, and Wangmeng Zuo. 2024b. Deblur4DGS: 4D Gaussian Splatting from Blurry Monocular Video. arXiv:2412.06424 [cs.CV] <https://arxiv.org/abs/2412.06424>
- Daniel Yang, John J. Leonard, and Yogesh Girdhar. 2024a. SeaSplat: Representing Underwater Scenes with 3D Gaussian Splatting and a Physically Grounded Image Formation Model. arXiv:2409.17345 [cs.CV] <https://arxiv.org/abs/2409.17345>
- Zeyu Yang, Hongye Yang, Zijie Pan, and Li Zhang. 2024b. Real-time Photorealistic Dynamic Scene Representation and Rendering with 4D Gaussian Splatting. In *The Twelfth International Conference on Learning Representations*. OpenReview.net, Vienna, Austria. <https://openreview.net/forum?id=WhgB5sisPv>
- Jinze Yu, Yiqun Wang, Zhengda Lu, Jianwei Guo, Yong Li, Hongxing Qin, and Xiaopeng Zhang. 2025. DehazeGS: Seeing Through Fog with 3D Gaussian Splatting. arXiv:2501.03659 [cs.CV] <https://arxiv.org/abs/2501.03659>
- Lingzhe Zhao, Peng Wang, and Peidong Liu. 2025. BAD-Gaussians: Bundle Adjusted Deblur Gaussian Splatting. In *Computer Vision – ECCV 2024*, Aleš Leonardis, Elisa Ricci, Stefan Roth, Olga Russakovsky, Torsten Sattler, and Gül Varol (Eds.). Springer Nature Switzerland, Cham, 233–250.

A Overview

Algorithm 1, summarizes our method overview with novel components highlighted in blue.

ALGORITHM 1: Overview

```

Input : Streaming multi-view images  $\tilde{I}_t^v$  at view  $v$  and time  $t$ 
Output: Optimized Gaussians  $G_t$  at time  $t$ 
 $t \leftarrow 0$ ; // video starts
 $G_0 \leftarrow \text{InitAttributes}(\text{SfM Points})$ ; // Initialize attributes
 $\{M_0^v | v \in V\} \leftarrow \text{InitResidualMap}()$ ; // Zero Init
while Gaussians  $G_0$  not converged do
   $\hat{I}_0^v \leftarrow \text{Rasterize}(G_0, v)$ ; // Rendering
   $\tilde{I}_0^v \leftarrow \tilde{I}_0^v - M_0^v$ ; // Restore (Figure 6)
   $L \leftarrow L_{\text{total}}(\hat{I}_0^v, \tilde{I}_0^v)$ ; // Loss (Eq. 3)
   $G_0, M_0^v \leftarrow \text{Adam}(\nabla L)$ ; // Backprop & Step (Eq. 2)
  if DensificationIteration then
    Densification(); // Prune & Split & Clone
  end
end
while multi-view video stream is not terminated do
   $G_{t+1} \leftarrow G_t$ ; // Initialize from previous Gaussians
  while Gaussians  $G_t$  not converged do
     $\hat{I}_{t+1}^v \leftarrow \text{Rasterize}(G_{t+1}, v)$ ; // Rendering
     $\tilde{I}_{t+1}^v \leftarrow \tilde{I}_{t+1}^v - M_{t+1}^v$ ; // Restore (Figure 6)
     $L \leftarrow L_{\text{total}}(\hat{I}_{t+1}^v, \tilde{I}_{t+1}^v)$ ; // Loss (Eq. 4)
     $G_{t+1}, M_{t+1}^v \leftarrow \text{Adam}(\nabla L)$ ; // Backprop & Step (Eq. 2)
  end
   $G_{t+1}^{\text{new}} \leftarrow \text{SpawnGaussians}(G_{t+1})$ ; // Spawn
  while new Gaussians  $G_{t+1}^{\text{new}}$  not converged do
     $\hat{I}_{t+1}^v \leftarrow \text{Rasterize}((G_{t+1}, G_{t+1}^{\text{new}}), v)$ ; // Rendering
     $\tilde{I}_{t+1}^v \leftarrow \tilde{I}_{t+1}^v - M_{t+1}^v$ ; // Restore (Figure 6)
     $L \leftarrow L_{\text{total}}(\hat{I}_{t+1}^v, \tilde{I}_{t+1}^v)$ ; // Loss (Eq. 4)
     $G_{t+1}^{\text{new}}, M_t^v \leftarrow \text{Adam}(\nabla L)$ ; // Backprop & Step (Eq. 2)
  end
   $t \leftarrow t + 1$ ; // next time step
   $G_t \leftarrow (G_t, G_t^{\text{new}})$ ; // reuse new gaussians
end

```

B Experiments Details

B.1 Implementation Details

We implemented our method within the official repositories of each baseline. For the initial frame reconstruction, we trained for 15000 iterations, with densification running up to 7500 iterations for SfM initialization and 5000 iterations for MVS initialization [Schonberger and Frahm 2016]. During training, we decayed the learning rate for residual maps from $1e-4$ to $1e-6$ for initial frame reconstruction and from $1e-5$ to $1e-7$ for sequential frame reconstruction. Both λ_{opa} and λ_{res} were set to 0.01. All models were trained with a single RTX A5000.

B.2 Modified Dynamic3DG

We modified several aspects of the original implementation of Dynamic3DG [Luiten et al. 2024] that were limiting performance. First,



Fig. 13. **Bounding Box of the Dynamic Region in the sear_steak Scene.**

instead of using SH degree 0 with per-camera colors to model view-dependent color, we increase the SH degree, as the original approach degraded temporal consistency. Second, we removed the velocity-based displacement initialization, which was causing artifacts. While Dynamic3DG optimizes color differently from the original paper, we do not optimize it to avoid excessive storage from a high SH degree. Instead we introduce a stage to train new Gaussians, which are then propagated to the next frame.

Dynamic3DG[†] achieves a PSNR of 32.48 on the Neural 3D Video dataset, surpassing the previously reported Dynamic3DG performance of 30.67 [Li et al. 2024a].

B.3 Details of Datasets

B.3.1 Sync-NeRF. To better distinguish between static and dynamic regions, we modified the scene to eliminate shadows. We then re-rendered the modified assets using the Cycles engine with 512 sample counts to remove rendering noise. We verified the absence of rendering noise by confirming that pixel values in static regions remained constant across all frames.

B.3.2 Measuring Total Variation in Static Regions. We manually created masks by defining bounding boxes around dynamic regions to measure total variation in the static regions, as shown in Figure 13.

C Additional Comparison

C.1 Experiments Details

The experimental settings of HiCoM [Gao et al. 2024] are different from previous works [Luiten et al. 2024; Sun et al. 2024]. We conducted additional experiments using original images and MVS initialization, even though image undistortion improves the PSNR. We measured the mean and standard deviation across all 10 runs without selection, labeling as “Online*”. In this setting, we additionally compare the performance of online reconstruction methods and offline reconstruction methods.

Table 4. **Additional Comparison with Offline Reconstruction.** For Online*, we report the average values across 10 runs.

Category	Model	Neural 3D Video		
		PSNR \uparrow	SSIM \uparrow	mTV $\times 100$ \downarrow
Offline	MixVoxels-L	30.81	0.933	0.000
	K-Planes-H	31.22	0.947	0.055
	4DGS	32.14	0.947	0.036
	4DGaussians	31.84	0.946	0.024
	STG	31.96	0.948	0.014
	E-D3DGS	32.10	0.951	0.026
Online*	Dynamic3DG \dagger	31.88	0.952	0.174
	Dynamic3DG \dagger + ours	32.61	0.955	0.077
	3DGStream	31.65	0.949	0.285
	3DGStream + ours	32.67	0.955	0.148
	HiCoM	31.61	0.948	0.193
	HiCoM + ours	31.75	0.948	0.129

Table 5. **Average Performance on Neural 3D Video Dataset without Image Undistortion.** We use the best initial frame reconstruction from 10 runs for sequential reconstruction, same as the main experiments.

Model	Neural 3D Video		
	PSNR \uparrow	SSIM \uparrow	mTV $\times 100$ \downarrow
Dynamic3DG \dagger	32.12	0.952	0.169
Dynamic3DG \dagger + ours	32.84	0.956	0.077
3DGStream	32.11	0.952	0.276
3DGStream + ours	32.90	0.956	0.146
HiCoM	32.03	0.950	0.198
HiCoM + ours	32.13	0.950	0.129

Offline Reconstruction. STG [Li et al. 2024a] originally reconstructs each video segment independently due to memory constraints, causing visual inconsistencies between segments. For a fair comparison, we modified the implementation of STG to train on the complete video, following 4D-Scaffold [Cho et al. 2024].

C.2 Comparison

Applying our method improves both temporal consistency (reduced mTV) and visual quality (increased PSNR) as shown in Table 4 and Table 5. Moreover, our method demonstrates greater stability with lower standard deviation than baselines, as shown by smaller ellipse radii in the scatter plot (Figure 14).

C.3 Comparison to Offline Reconstruction

3DGStream with our methods achieves the best visual quality among online and offline methods. However, our method enhances the temporal consistency of online methods, it does not reach the consistency level of offline methods. Our best results show 1.4 \times higher total variation compared to the worst offline reconstruction, thus it does not yet match offline methods. We attribute the gap to the nature of online configuration, which uses only a snapshot at a

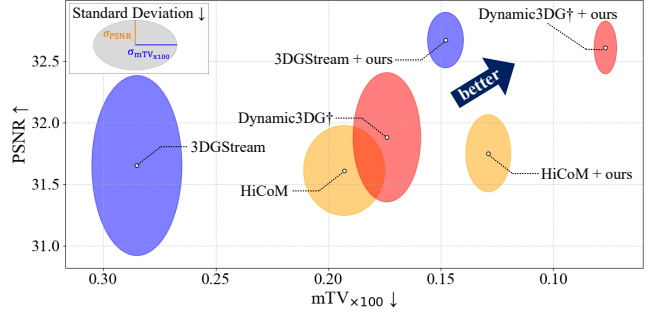


Fig. 14. **Scatter Plots Across 10 Runs for each Scene in the Neural 3D Video Dataset.** The radii of the ellipse represent the standard deviations along each axis.

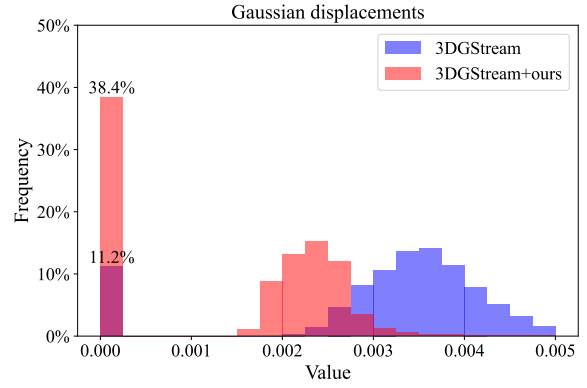


Fig. 15. **Histogram of Gaussian Displacements in the coffee_martini Scene.**

moment without the previous and next frames, leading to inevitable occlusions.

C.4 Comparison to V^3

V^3 [Wang et al. 2024] proposes temporal entropy loss and temporal loss to enhance temporal continuity, leading to efficient compression. These losses are L2 regularization and entropy regularization on the scale, rotation, and opacity displacement of Gaussians¹⁰.

However, V^3 targets only the reconstruction of dynamic foregrounds and does not handle static backgrounds. Therefore, our method is orthogonal to V^3 , which makes it unsuitable for demonstrating our effectiveness in enhancing temporal consistency in static regions. Moreover, V^3 applies the loss only within groups, without considering temporal continuity across groups, which makes it limited.

Therefore, instead of directly comparing with V^3 , we compare against its proposed loss. In Table 6, our method outperforms loss of V^3 , demonstrating superior effectiveness.

¹⁰Unlike the original paper, their implementation does not apply loss to the color (<https://github.com/AuthorityWang/VideoGS>).

Table 6. Comparison to Temporal Loss on Neural 3D Video Dataset.

Model	PSNR \uparrow	SSIM \uparrow	mTV $_{\times 100}$ \downarrow
3DGStream	32.58	0.960	0.178
3DGStream + V^3 loss	32.57	0.960	0.180
3DGStream + ours	33.13	0.961	0.103

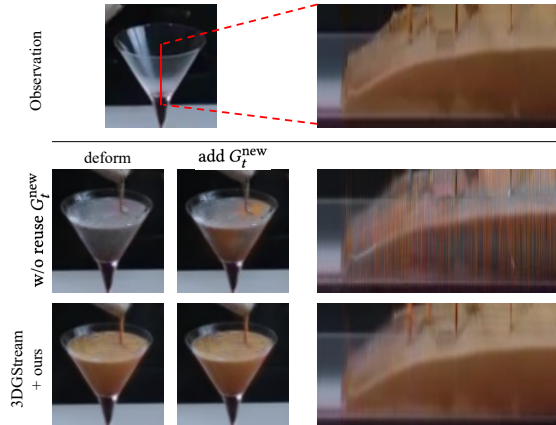
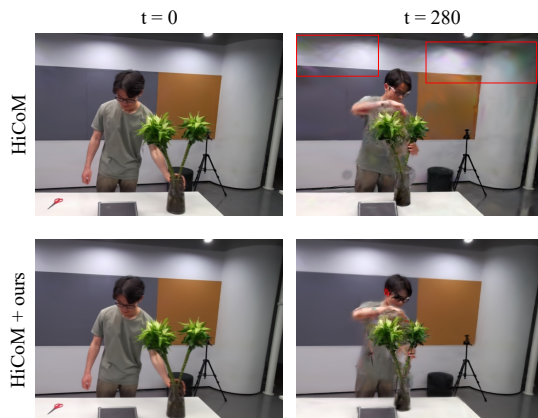
Fig. 16. Difference in Temporal Consistency with and without Reusing New Gaussians G_t^{new} in Subsequent Frames.

Fig. 17. HiCoM Exhibits Limited Static Region Preservation.

D More Analysis

D.1 Displacement Distribution

To demonstrate the movement of Gaussian over time, we compared 3DGStream with and without our method. Figure 15 shows the histogram distribution of Gaussian position displacements. Our method increases the number of Gaussians with near-zero displacement by 3.4 \times compared to the baseline, indicating a substantial reduction in unnecessary motion of static Gaussians. This leads to more accurate scene representation and better temporal consistency in static regions.

Table 7. Effect of Noise Levels on Temporal Inconsistency. We report mTV $_{\times 100}$ on Sync-NeRF dataset.

Noise level (mTV $_{\times 100}$)	0.452	0.908	1.840
3DGStream	0.483	0.559	0.887
3DGStream + ours	0.318 (0.66 \times)	0.452 (0.81 \times)	0.815 (0.92 \times)

Table 8. Effect of Number of Train Views on Temporal Inconsistency. We report mTV $_{\times 100}$ on Sync-NeRF dataset.

Number of views	13	9	5
3DGStream	0.483	0.764	0.924
3DGStream + ours	0.318 (0.66 \times)	0.645 (0.84 \times)	0.829 (0.90 \times)

D.2 New Gaussians and Temporal Consistency

We demonstrate that using new Gaussians only in a specific frame harms temporal consistency. As shown in Figure 16, the coffee exhibits temporal inconsistency in “w/o reuse G_t^{new} ”. This occurs because Gaussians representing glass are deformed to represent coffee in subsequent frames, disrupting the optimization of new Gaussians. We show that this issue is resolved by propagating new Gaussians to subsequent frames in “3DGStream+ours”.

D.3 Additional Comparison to HiCoM

Our experiments show that both the original HiCoM and HiCoM with our method fail to reconstruct fast motions as discussed in the limitation. However, Figure 17 shows that our method performs notably better quality in static regions while the original HiCoM fails to preserve the quality of static regions.

D.4 Various Noise Levels

Noises in adjacent frames differ according to devices and environments. In our experiments, the observations are captured by various devices (GoPro and Kinect) and various environments. Their temporal inconsistency varies in [0.090,0.834].

As shown in Table 7, our method improves temporal consistency under various noise levels, though the improvement decreases with severe noise.

D.5 Various Number of Train Views

In Table 8, we validate our method under the number of training views. While our method improves temporal consistency across various number of training views, its effectiveness decreases as the number of views is reduced, since it relies on well-reconstructed scenes and multi-view consistency of Gaussians to fit multi-view inconsistent noise.

E More Results

We report the quantitative results of each scene in Table 9. Our method enhances temporal consistency across all scenes (reduced mTV). We report per-frame metrics in Figure 18, where our method outperforms the baseline in most cases.

Table 9. Per-scene Quantitative Results on Neural 3D Video and Meetroom Dataset. We report mean \pm standard deviation of video frames.

Model	coffee_martini			cook_spinach			cut_roasted_beef		
	PSNR \uparrow	SSIM \uparrow	mTV $\times 100$ \downarrow	PSNR \uparrow	SSIM \uparrow	mTV $\times 100$ \downarrow	PSNR \uparrow	SSIM \uparrow	mTV $\times 100$ \downarrow
Dynamic3DG \dagger	29.36 \pm 0.06	0.938 \pm 0.001	0.169 \pm 0.027	33.86 \pm 0.33	0.968 \pm 0.001	0.127 \pm 0.018	33.67 \pm 0.67	0.969 \pm 0.003	0.226 \pm 0.050
Dynamic3DG \dagger + ours	29.38 \pm 0.06	0.939 \pm 0.001	0.057 \pm 0.071	34.34 \pm 0.41	0.966 \pm 0.002	0.048 \pm 0.034	34.66 \pm 0.36	0.969 \pm 0.002	0.059 \pm 0.035
3DGStream	29.24 \pm 0.09	0.938 \pm 0.001	0.163 \pm 0.034	33.96 \pm 0.36	0.966 \pm 0.002	0.179 \pm 0.032	33.99 \pm 0.19	0.968 \pm 0.002	0.165 \pm 0.039
3DGStream + ours	29.54 \pm 0.06	0.941 \pm 0.001	0.082 \pm 0.070	34.52 \pm 0.38	0.967 \pm 0.002	0.105 \pm 0.035	34.78 \pm 0.19	0.968 \pm 0.002	0.097 \pm 0.039
HiCoM	29.14 \pm 0.09	0.936 \pm 0.001	0.256 \pm 0.026	33.39 \pm 0.50	0.961 \pm 0.003	0.140 \pm 0.023	34.00 \pm 0.27	0.965 \pm 0.003	0.119 \pm 0.027
HiCoM + ours	29.26 \pm 0.12	0.937 \pm 0.002	0.159 \pm 0.018	33.80 \pm 0.49	0.962 \pm 0.003	0.083 \pm 0.012	34.02 \pm 0.39	0.964 \pm 0.003	0.089 \pm 0.014

Model	flame_salmon			flame_steak			sear_steak		
	PSNR \uparrow	SSIM \uparrow	mTV $\times 100$ \downarrow	PSNR \uparrow	SSIM \uparrow	mTV $\times 100$ \downarrow	PSNR \uparrow	SSIM \uparrow	mTV $\times 100$ \downarrow
Dynamic3DG \dagger	29.70 \pm 0.13	0.940 \pm 0.001	0.145 \pm 0.028	33.88 \pm 0.54	0.973 \pm 0.001	0.123 \pm 0.027	34.42 \pm 0.15	0.974 \pm 0.001	0.126 \pm 0.018
Dynamic3DG \dagger + ours	29.75 \pm 0.16	0.942 \pm 0.001	0.053 \pm 0.062	35.03 \pm 0.45	0.973 \pm 0.001	0.051 \pm 0.046	35.01 \pm 0.24	0.974 \pm 0.001	0.051 \pm 0.033
3DGStream	29.67 \pm 0.13	0.941 \pm 0.001	0.205 \pm 0.046	34.29 \pm 0.43	0.973 \pm 0.001	0.177 \pm 0.045	34.34 \pm 0.26	0.973 \pm 0.001	0.180 \pm 0.040
3DGStream + ours	29.99 \pm 0.11	0.944 \pm 0.001	0.116 \pm 0.061	34.86 \pm 0.37	0.973 \pm 0.001	0.103 \pm 0.046	35.11 \pm 0.20	0.974 \pm 0.001	0.113 \pm 0.036
HiCoM	29.46 \pm 0.26	0.939 \pm 0.003	0.218 \pm 0.056	32.48 \pm 0.37	0.968 \pm 0.001	0.111 \pm 0.014	34.08 \pm 0.22	0.971 \pm 0.001	0.137 \pm 0.019
HiCoM + ours	29.59 \pm 0.65	0.939 \pm 0.007	0.153 \pm 0.065	34.07 \pm 0.61	0.969 \pm 0.002	0.091 \pm 0.014	34.44 \pm 0.37	0.970 \pm 0.002	0.100 \pm 0.016

Model	discussion			trimming			vrheadset		
	PSNR \uparrow	SSIM \uparrow	mTV $\times 100$ \downarrow	PSNR \uparrow	SSIM \uparrow	mTV $\times 100$ \downarrow	PSNR \uparrow	SSIM \uparrow	mTV $\times 100$ \downarrow
Dynamic3DG \dagger	31.32 \pm 0.36	0.956 \pm 0.002	0.192 \pm 0.019	31.73 \pm 0.19	0.953 \pm 0.001	0.173 \pm 0.011	29.32 \pm 0.95	0.948 \pm 0.003	0.158 \pm 0.011
Dynamic3DG \dagger + ours	31.95 \pm 0.96	0.959 \pm 0.003	0.145 \pm 0.137	31.66 \pm 0.25	0.952 \pm 0.002	0.127 \pm 0.037	30.27 \pm 1.13	0.949 \pm 0.004	0.107 \pm 0.031
3DGStream	31.78 \pm 0.30	0.956 \pm 0.003	0.055 \pm 0.009	32.29 \pm 0.21	0.957 \pm 0.001	0.039 \pm 0.008	31.14 \pm 0.19	0.953 \pm 0.001	0.052 \pm 0.001
3DGStream + ours	32.51 \pm 0.36	0.958 \pm 0.002	0.027 \pm 0.004	32.78 \pm 0.20	0.958 \pm 0.001	0.018 \pm 0.004	31.58 \pm 0.35	0.953 \pm 0.002	0.027 \pm 0.000
HiCoM	29.02 \pm 1.56	0.929 \pm 0.017	0.166 \pm 0.075	29.48 \pm 1.14	0.936 \pm 0.011	0.131 \pm 0.070	29.75 \pm 0.67	0.943 \pm 0.004	0.083 \pm 0.014
HiCoM + ours	28.87 \pm 0.73	0.931 \pm 0.008	0.056 \pm 0.011	29.69 \pm 0.82	0.940 \pm 0.006	0.044 \pm 0.015	29.71 \pm 0.50	0.941 \pm 0.003	0.047 \pm 0.005

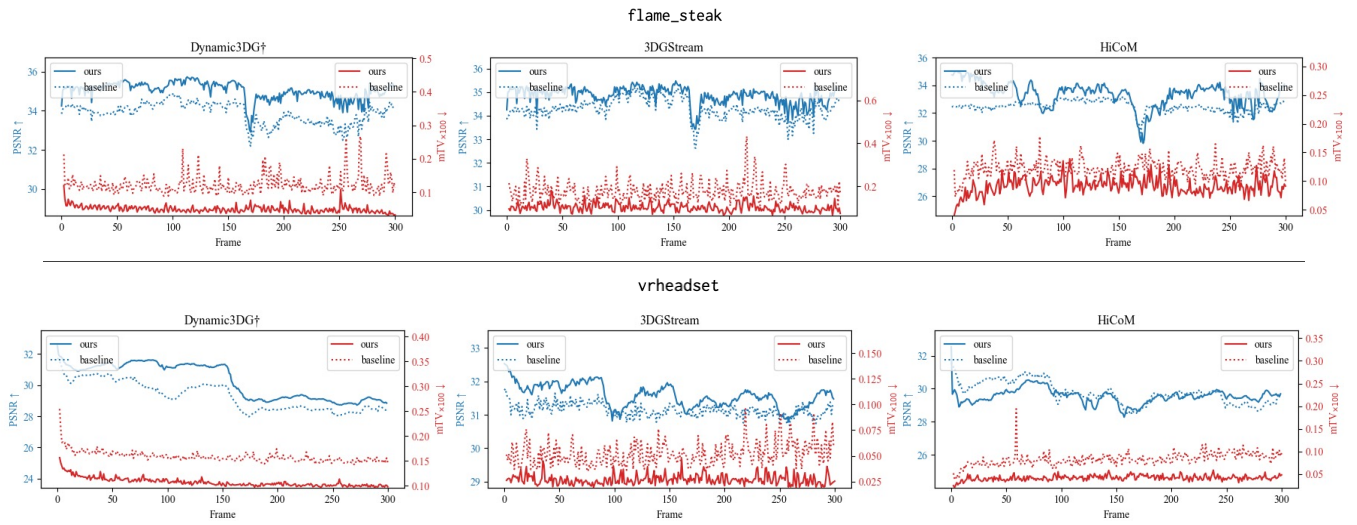


Fig. 18. Per-frame Metrics of flame_steak and vrheadset Scene.